Applied Surface Science 579 (2022) 152249

Contents lists available at ScienceDirect

Applied Surface Science

journal homepage: www.elsevier.com/locate/apsusc

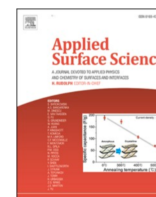

Full Length Article

Controllable synthesis of Si-based GeSn quantum dots with room-temperature photoluminescence

Lu Zhang, Haiyang Hong, Kun Qian, Songsong Wu, Guangyang Lin, Jianyuan Wang, Wei Huang, Songyan Chen, Cheng Li *

Semiconductor Photonics Research Center, Department of Physics, Xiamen University, Xiamen, Fujian 361005, People's Republic of China

ARTICLE INFO

Keywords:
GeSn quantum dots
Room-temperature photoluminescence
Silicon photonics
Quantum confinement effect

ABSTRACT

GeSn quantum dots (QDs) are regarded as a promising material to improve the performance of GeSn lasers. However, developing a complementary-metal-oxidesemiconductor (CMOS) compatible approach to prepare GeSn QDs is the main bottleneck at present. In this work, we demonstrate a highly controllable method for the synthesis of GeSn QDs in a CMOS compatible way. Ultra-high area density 2.1×10^{12} cm^{-2}, high-Sn fraction 44.2%, and narrow distributed size of the GeSn QDs is obtained. Furthermore, evident quantum confinement effect is observed from the absorption and room-temperature photoluminescence spectra. The properties of the GeSn QDs can well be controlled by merely adjusting the preparation temperature. Moreover, the synthesis mechanism of the GeSn QDs is comprehensively analyzed and revealed using classical nucleation theory and first-principles calculation. The feasible and CMOS compatible method with high controllability may provide a promising way to obtain highly efficient Si-based light emitting materials, and may further be applied in other group-IV alloys, such as SiSn, SiGeSn, SiPb, and GePb.

1. Introduction

Direct bandgap GeSn alloys are regarded as one of the most promising materials for the realization of complementary-metal-oxidesemiconductor (CMOS) compatible light source, which is the only unsolved component of silicon-based optoelectronic integration circuits (OEICs) up to date. Especially, GeSn lasers are in a period of rapid development as their performance was successively improved in recent years [1–6]. Nevertheless, the low operating temperature and high lasing threshold impede further application of the reported GeSn lasers. The main cause of this problem is recently revealed to be resulted from the intrinsic limitation of bulk GeSn alloys [7]. Therefore, finding a way to breakthrough this natural constrain is vital and urgent. Downscaling the bulk GeSn alloys to low-dimensional structures such as, quantum wells [8–10], quantum wires [11–14], and QDs, are supposed to be a feasible way to effectively improve the efficiency of light emission. The improvement is ascribed to the reduction of free carrier absorption and enhanced light gain due to quantum confinement effect, which is most pronounced in QDs among the nanostructures. Therefore, GeSn QDs are now coming into notice. To date, several works related to the preparation of GeSn QDs or nanocrystals are reported [15–22]. Most of the preparation methods are based on the colloidal by means of chemical reduced reactions except for some CMOS compatible ways. Note that the GeSn nanocrystals discussed here are referred to those of individually separated nanocrystals rather than those of polycrystalline GeSn films with nanoscale grains [23,24]. We have reported a work related to the preparation of the GeSn QDs, which is to date the only one CMOS compatible method that can obtain high crystallinity as well as room-temperature photoluminescence [22]. However, the reported experiment contains only one preparation condition, leaving the synthesis mechanism and controllability of the GeSn QDs remain elusive.

In this work, the preparation of GeSn QDs with more preparation conditions are carried out, the controllability and mechanism of the synthesis are demonstrated and revealed. The fabricated GeSn QDs are uniformly distributed in the amorphous GeSn (a-GeSn) film. Besides, the narrow size distribution and the ultra-high area densities of the GeSn QDs are presented. It is found that the Sn fraction of the GeSn QDs is much higher than that of the surrounded a-GeSn. Owing to this spontaneous form of heterostructure, a type-I electronic band alignment may be constructed. And this should be one of the key factors for the occurrence of room-temperature photoluminescence, which presents the high efficiency of light emission. The Sn fraction, size and area

* Corresponding author.
E-mail address: lich@xmu.edu.cn (C. Li).

https://doi.org/10.1016/j.apsusc.2021.152249
Received 2 October 2021; Received in revised form 22 November 2021; Accepted 15 December 2021
Available online 18 December 2021
0169-4332/© 2021 Elsevier B.V. All rights reserved.

density of the GeSn QDs can be well controlled by merely adjusting the preparation temperature. The synthesis mechanism of the GeSn QDs including the nucleation, growth, and ripening stages is systematically analyzed and revealed with evidences provided by the classical nucleation theory (CNT) and first-principles calculations. It is found that the growth of GeSn QDs is motivated by the tendency of reduction of Gibbs free energy, which is dominated by the surface energy during the nucleation and growth stages. And the ripening of GeSn QOs is ascribed to the strain induced increment of Gibbs free energy surpass the thermal energy. The controllability of the feasible synthesis method for the preparation of the GeSn QDs may provide a promising way for the realization of Si-based lasers with high emission efficiency and high

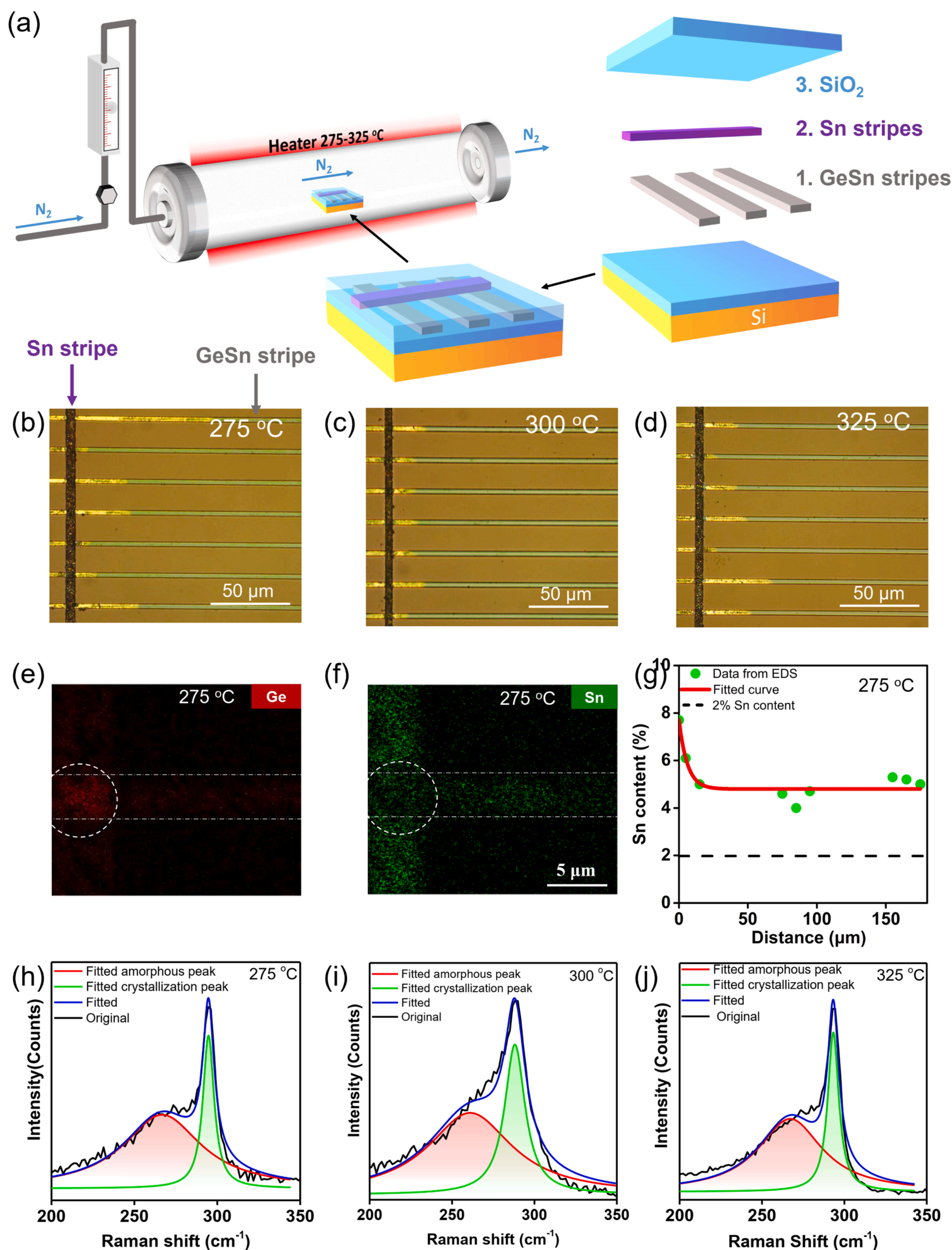

Fig. 1. (a) Schematic illustration of the preparation process of GeSn QDs. (b-d) The top-view OM images of the samples after annealing for 40 h at 275, 300, and 325 °C, respectively. (e, f) The Ge (e) and Sn (f) EDS element mappings for the sample after annealing at 275 °C for 40 h. (g) The Sn density distribution along GeSn strip for the sample after annealing at 275 °C for 40 h. (h-j) The Raman spectra of the samples in the non-obvious-inter-diffusion regions after annealing for 40 h at 275, 300, and 325 °C, respectively.

operation temperature. And the synthesis method may further be applied to other alloys, for instance, SiSn, SiGeSn, SiPb or GePb.

2. Experimental

Firstly, Si substrates with 300 nm thick SiO_2 on the top are cleaned by the acetone and the absolute ethyl alcohol followed with the rinse of deionized water. Then amorphous GeSn (a-GeSn) stripes with the width of 3.6 μm, length of 200 μm, and thickness of 50 nm are patterned and deposited on the substrates by lithography and lift-off process and by magnetron sputtering technique, respectively. Co-sputtering of Sn and Ge is implemented for the deposition of GeSn stripes with the sputtering pressure of 0.5 Pa in Ar ambient. The purities of the Sn and Ge targets are 0.9999 and 0.99999, respectively. The initial Sn content of the a-GeSn stripes is 2% by adjusting the sputtering power ratio between the Sn and Ge targets. Next, the Sn stripes with the width of 4.3 μm are deposited orthogonally on the top of the a-GeSn and near one end of the a-GeSn about 20 μm. The patterning and deposition of the Sn stripes are also based on lithography and lift-off process and sputtering technique, respectively. After that, a layer of 500 nm SiO_2 is deposited on the top by plasma enhanced chemical vapor deposition technique. And finally, the samples are annealed at 275, 300 and 325 °C for 40 h, respectively, with N_2 atmosphere in a tube furnace. The preparation process is schematically illustrated in Fig. 1a.

Optical microscopy (OM) is implemented to observe the top view of the samples. Raman measurements are performed on a commercial system Labram HR Evolution using a 532 nm laser for excitation. The optical bandgaps of the prepared GeSn nanocrystals are characterized by the absorbance spectroscopy and photoluminescence spectroscopy. Photoluminescence measurements are carried out in a module embedded in the Labram HR Evolution at room temperature with 532 nm excitation laser. Absorbance measurements are performed using a Cary 5000 UV–vis-NIR spectrophotometer. The diffusion of Sn along the GeSn stripes is characterized by the energy dispersive spectroscopy (EDS) equipped in scanning electron microscopy (SEM). The crystalline morphology is characterized by transmission electron microscopy (TEM), high-resolution TEM (HRTEM) and selected area electron diffraction (SAED). Energy dispersive X-ray (EDX) spectroscopy quipped in the TEM is applied to detect the distribution of Sn and Ge elements in the GeSn stripes.

3. Results and discussion

Fig. 1b-d show the top-view images of the after-annealing samples by optical microscopy (OM). The horizontal green stripes and vertical brown stripes are GeSn and Sn stripes, respectively. The bright yellow region of the GeSn stripes near the Sn stripes results from the drastic inter-diffusion between the GeSn and Sn stripes. The energy dispersive spectroscopy (EDS) elemental mapping images also illustrate the inter-diffusion behaviour, as shown in Fig. 1e, f. The GeSn stripes annealed at 275 °C is taken as an example, the EDS results of the other samples are similar and not shown here. In order to probe the variation of Sn fraction along the GeSn stripes, the atomic ratio of Sn along the GeSn stripes are collected, as shown in Fig. 1g. A red curve is fitted to the collected EDS data (green dots), and a black dash line, which denotes as the initial Sn content in the a-GeSn stripes, is also presented as reference. The 0 μm distance means the position is just at the edge of Sn stripe. It can be observed that in the obvious inter-diffusion region, the Sn content gradually decreases away from the Sn stripe. As the distance larger than the obvious inter-diffusion length, the Sn content slightly fluctuates around 5%, which is higher than the initial of the GeSn stripe, indicating a homogeneous increment of Sn atoms diffused from the Sn stripe.

All the obvious inter-diffusion regions of the GeSn stripes in the samples are revealed to be high crystalline while the remain regions in each sample are mixture of amorphous and crystalline GeSn as revealed by the Raman spectra. For a given sample, no significant difference is observed for the amorphous and crystalline peaks at different position in the non-obvious-inter-diffusion regions. Fig. 1(h-j) show the representative Raman spectra in the non-obvious-inter-diffusion regions for samples annealed at 275, 300, and 325 °C, respectively. The spectra are decomposed to an amorphous peak (red) and a crystalline peak (green) with Lorentzian shape. The crystallinities of the samples are 23.1, 32.6 and 38.3% for samples annealed at 275, 300, and 325 °C, respectively, reflecting the mixture state of amorphous and crystalline. The crystallinity is defined as the integral area ratio of the crystalline peak to that of the whole Raman spectrum. The evident red shift of the crystalline peaks relative to bulk Ge of 300.4 cm^{-1} proves the incorporation of Sn atoms into Ge lattice.

Fig. 2a shows the cross-sectional TEM image of GeSn stripe after 275 °C annealing. At the low resolution, a SiO_2/GeSn/SiO_2 sandwich structure can be observed. The thickness of the GeSn stripe is measured to be about 55 nm. Some darker dots are uniformly distributed in the GeSn layer. Implementing HRTEM, the details of the crystallization morphology is further investigated. As shown in the left of Fig. 2b, the darker dots are revealed to be spherical nanocrystals (highlighted by white dash circle) with complete and regular lattice pattern, manifesting the high crystallinity of the nanocrystals. The rest regions are revealed to be amorphous as shown in the right of Fig. 2b. Moreover, the absence of segregation and precipitation of Sn in the nanocrystals also confirms the excellent crystallization property. However, the rest region of the GeSn layer, of which the color is light grey in Fig. 2a, remains amorphous. Fig. 2c shows the SAED patterns of the GeSn layer. Due to the characterization area under SAED covering a certain range, the SAED pattern presents the information including multiple nanocrystals and amorphous in the area. The cooccurrence of the crystal diffraction spots and the amorphous diffraction ring further confirms the mixture of crystalline and amorphous. The diffraction spots are proof to result from the (2 2 0) plane of the GeSn nanocrystals. And the Sn fraction of the GeSn nanocrystals evaluated to be 44.2%, which is much higher than that of the initial Sn fraction in the as deposited GeSn. The Sn fraction calculated by the interplanar spacing from the HRTEM images consists with that from the SAED. And there is little difference in Sn fraction among the GeSn nanocrystals. The high Sn fraction of the GeSn nanocrystals can result in the darker color of the GeSn nanocrystals in Fig. 2(a). Since Sn atom is larger and heavier than Ge atom, the more electrons around the atom increase the scattering probability of electrons ejected from the equipment, and decrease the quantity of the transmission electron. Moreover, the formation of crystal can also decrease the quantity of the transmission electron due to the coherent diffraction. And the large contrast between the amorphous and the nanocrystals indicates the lower Sn fraction in the amorphous. Further confirmation is made by the results from the EDX spectroscopy, as shown in Fig. 2d. On the top left of the figure, the high angle annular dark field (HAADF) image has the color inverse with Fig. 2a. The top right of Fig. 2d shows the superimposed element mapping of the Sn and the Ge. To intuitively distinguish the distribution of the elements, the individual mapping of the Sn and the Ge are presented on the down left and down right of the figure, respectively. The Ge atoms are uniformly distributed in the GeSn layer while the Sn atoms appear to concentrate on small dot like regions, which corresponds to the GeSn nanocrystals. In addition, the Sn atoms in the amorphous are too little to be detected as shown in the Sn element mapping of Fig. 2 (d). This result demonstrates that the Sn atoms in the Sn stripe diffuse into the GeSn stripe and spontaneously gather together at places where the GeSn nanocrystals form, because a higher Sn fraction in the a-GeSn will induce the crystallization of the a-GeSn [25,26]. Fig. 2e shows the size of the GeSn nanocrystals distribute in a narrow span 2.5–4.5 nm, indicating the uniformity of the GeSn nanocrystals. The average size is evaluated to be about 3 nm, and the full width at half maximum (FWHM) of the size distribution fitted by Gaussian curve is 2.1 nm. And the area density of the GeSn nanocrystals is evaluated to an ultra-high level of 2.1×10^{12} cm^{-2}.

Fig. 3a shows the cross-sectional TEM image of GeSn stripe after

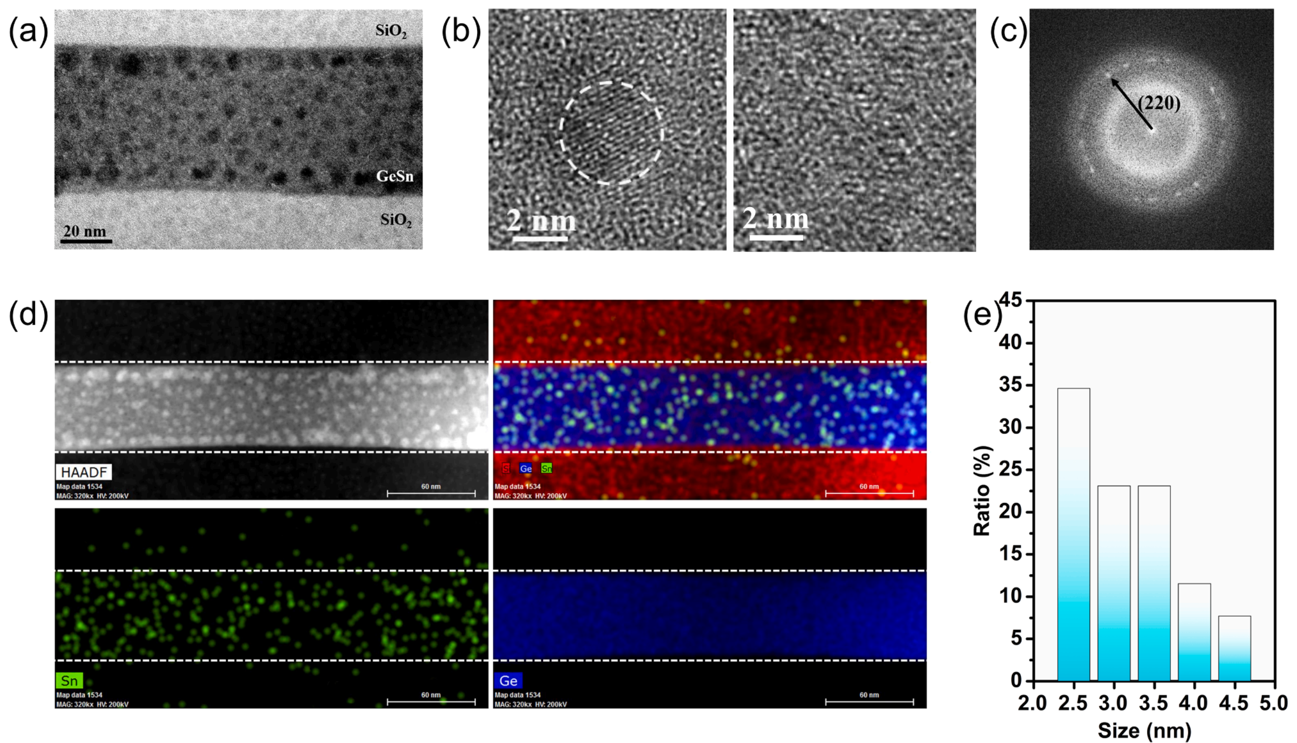

Fig. 2. (a) Cross-section TEM image of the sample after annealed at 275 °C for 40 h. (b) HRTEM image of the GeSn nanocrystals (left) and the amorphous region (right). (c) SAED patterns of the sample after annealed at 275 °C for 40 h. (d) EDX element mappings for the sample after annealed at 275 °C for 40 h. (e) Histogram of the fraction for nanocrystals size distribution. The FWHM of the size distribution fitted by Gaussian curve is 2.1 nm.

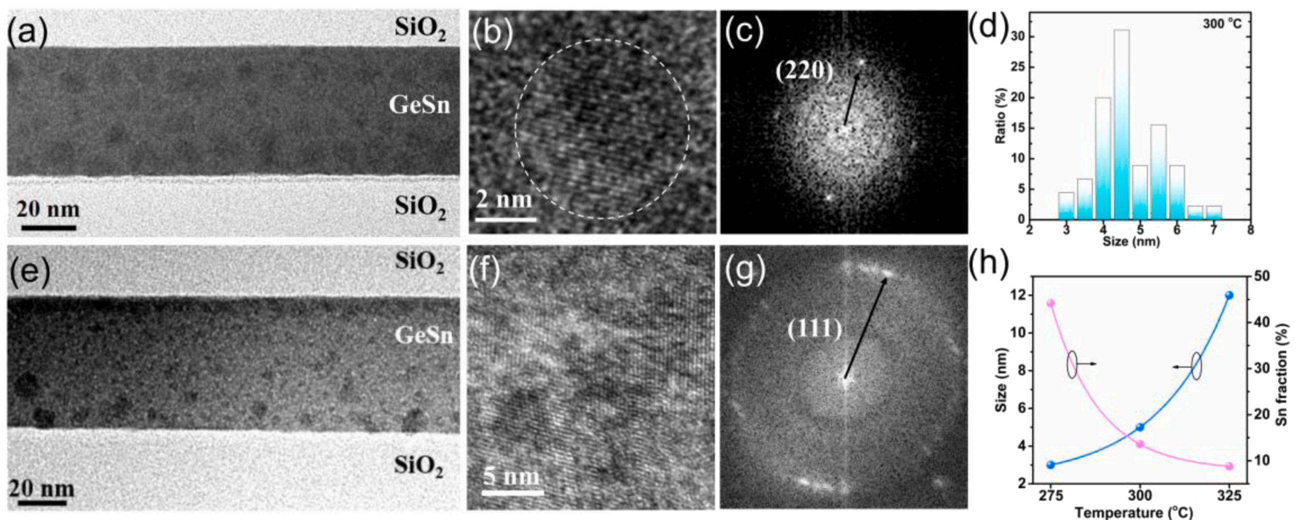

Fig. 3. (a, e) Cross-section TEM images of the sample after annealed for 40 h at 300 °C (a) and 325 °C (e). (b, f) HRTEM images of the GeSn nanocrystals annealed for 40 h at 300 °C (b) and 325 °C (f). (c, g) FFT patterns taken from the nanocrystals annealed for 40 h at 300 °C (c) and 325 °C (g). (d) Histogram of the fraction for nanocrystals size distribution of the sample after annealed for 40 h at 300 °C. The FWHM of the size distribution fitted by Gaussian curve is 1.7 nm. (h) The nanocrystals size and the Sn fraction dependence on annealing temperature.

300 °C annealing. Some darker dots are uniformly distributed in the GeSn layer, similar to that of the 275 °C annealing sample. The HRTEM images in Fig. 3b clearly shows the complete and regular plane, and no any Sn cluster is presence as well. Fast Fourier transformation (FFT) is implemented to calculate the diffraction pattern, as shown in Fig. 3c. The amorphous ring and crystal spots cooccur as well. The spots are distinguished as the result of (220) plane, and the Sn fraction in the GeSn nanocrystals is computed to be 12.9%, which is also much higher than that of the initial Sn fraction in the as deposited GeSn but lower than that of the 275 °C annealing sample. The statistics of the size of the nanocrystals are plotted in Fig. 3d, the size also spans a narrow range from 3 to 7 nm, and centralizes on 4–6 nm. The average size is about 5 nm, which is larger than that of the sample annealed at 275 °C. The FWHM of the size distribution fitted by Gaussian curve is 1.7 nm. Moreover, the area density of the GeSn nanocrystals is estimated to be 5.5×10^{11} cm^{-2}, lower than that of the sample annealed at 275 °C.

As the preparation temperature lifts to 325 °C, the size of the GeSn nanocrystals becomes bigger, resulting in the coalescence of the

nanocrystals and forming polycrystalline. Fig. 3e shows the cross-sectional TEM image at low-resolution. Some darker dots can be observed as well. However, these dots have less extent of size uniformity than that of the previous two samples and the distribution in the GeSn layer is uneven either. Most of the crystallization parts of the GeSn layer become polycrystalline due to the coalescence of the nanocrystals, as shown in Fig. 3f. No any Sn clusters presence as well. The FFT pattern of the 325 °C annealing sample consists of the amorphous diffraction ring and (1 1 1) diffraction spots, as shown in Fig. 3g. The Sn fraction of the crystalline GeSn is calculated to be 8.8%, still higher than that of the initial Sn fraction in the as deposited GeSn but lower than those of 275 and 300 °C annealing samples. However, the polycrystalline nature and inadequate Sn fraction may limit the achievement of direct bandgap and the application of lasers [27]. Although the crystallization region is predominated by polycrystalline, the size of the nanocrystals can be measured between their boundaries. The average size of the GeSn nanocrystals is computed to be about 12 nm, higher than those of the previous two samples. The FWHM of the size distribution fitted by Gaussian curve is 5.4 nm.

Hereto, we demonstrate a feasible method to prepare high-Sn fraction GeSn nanocrystals with uniform size distribution and high area density embedded in amorphous GeSn with low Sn fraction. One of the key advantages of the method is that the preparation process is CMOS compatible, which is vital for Si-based OEICs. In each of the samples with the separated GeSn nanocrystals, the Sn fraction of the nanocrystals is consistent. The narrow-distributed size and highly consistent Sn fraction promise a homogeneous property of the GeSn nanocrystals. Furthermore, the Sn fraction, size and area density of the GeSn nanocrystals can be well controlled by merely adjusting the annealing temperature. It is found that the Sn fraction of the GeSn nanocrystals decreases with the temperature while their size increases instead, as shown in Fig. 3h. The facile technique proposed here provides a new strategy for the synthesis of semiconductor alloys with high controllability in a CMOS compatible way.

The optical bandgaps of the prepared GeSn nanocrystals are characterized by the absorbance spectroscopy and photoluminescence spectroscopy. As shown in Fig. 4a, the absorption edges of 275 and 300 °C annealing samples can be well fitted by the relationship $(\alpha\hbar\nu)^2 \propto (\hbar\nu - E_g^{\Gamma})$, which represents direct bandgap absorption. $\alpha, \hbar, \nu$ and E_g^{Γ} are the absorption coefficient, Plank constant, angular frequency of the photon and direct bandgap of the GeSn nanocrystals, respectively. The extrapolated bandgaps for absorption are estimated to be 0.74 and 0.77 eV for 275 and 300 °C annealing samples, respectively. And their absorption coefficients for photon with energy larger than the bandgaps are more than 10^5 cm^{-1}, an order of magnitude higher than that of Ge. The evidences suggest that the prepared GeSn nanocrystals in 275 and 300 °C annealing samples are direct bandgap materials. However, for 325 °C annealing sample, the absorption spectrum decreases slowly and there is no obvious direct absorption edge. It agrees well with the relationship $(\alpha\hbar\nu)^{1/2} \propto (\hbar\nu - E_g^{L})$, which presents indirect bandgap absorption, as shown in Fig. 4b. E_g^{L} is the indirect bandgap and is extrapolated to be 0.56 eV, which consists with the calculated indirect bandgap 0.55 eV of bulk GeSn with Sn fraction of 8.8% (Supplementary material). However, the bandgaps of bulk GeSn with Sn fraction of 44.2 and 12.9% are estimated to be −0.213 and 0.426 eV (Supplementary material), respectively, much lower than that of the bandgaps extrapolated from the absorption data. As quantum confinement effect is taken into account, the bandgaps of GeSn nanocrystals of 275 and 300 °C annealing samples are evaluated to be 0.749 and 0.766 eV (Supplementary material), respectively, in agreement well with the extrapolated results. In other words, the prepared GeSn nanocrystals of 275 and

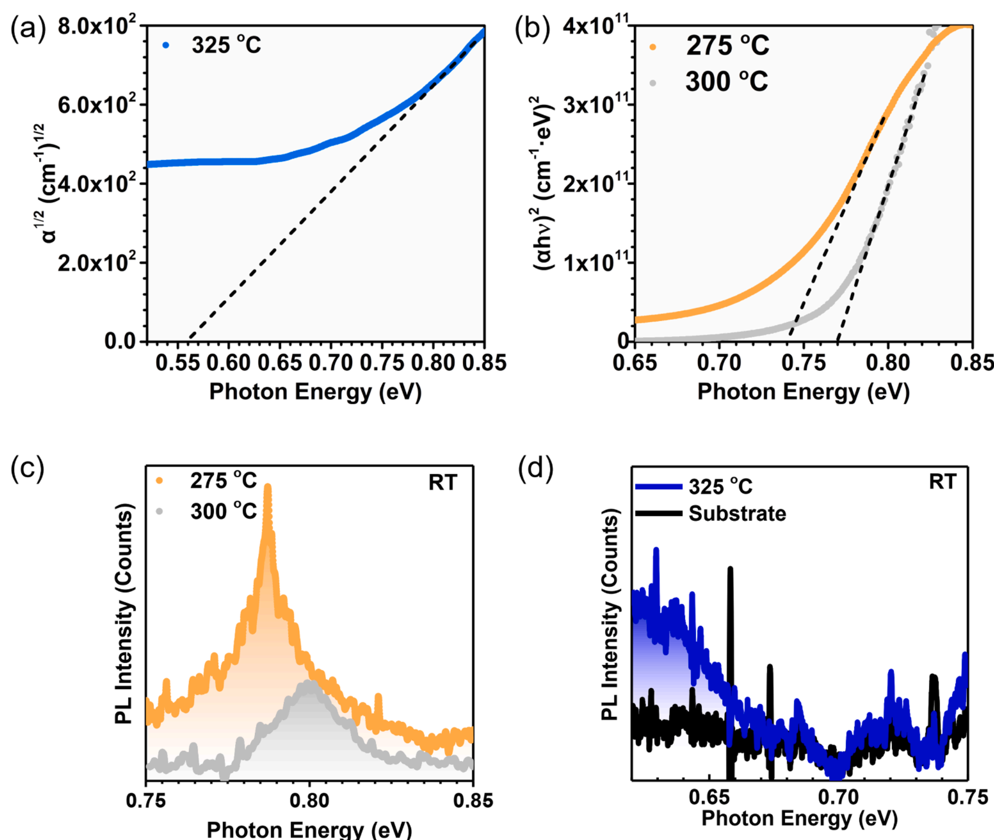

Fig. 4. (a) The data fitting of absorption edge for indirect bandgap energy of the sample after annealed at 325 °C for 40 h. (b) The data fitting of absorption edge for direct bandgap energy of the samples after annealed at 275 °C (wheat) and 300 °C (grey) for 40 h. (c) RT PL spectra of the samples after annealed at 275 °C (wheat) and 300 °C (grey) for 40 h.

300 °C annealing samples are GeSn QDs, since their bandgaps are extended largely by quantum confinement effect. While that of 325 °C annealing sample is polycrystalline with nanoscale grains.

Fig. 4c shows the room-temperature photoluminescence of the samples annealed at 275 and 300 °C. The peak of the 275 °C annealing sample lies at 0.787 eV and that of the 300 °C annealing sample shifts to 0.8 eV, both the peak positions are in good agreement with bandgap values extracted from the absorption spectra and calculation. Ultra-narrow full widths at half maximum (FWHM) of the spectra are obtained, 21 and 20 meV for 275 and 300 °C annealing samples, respectively, proving the high uniformity and excellent light emission rate of the GeSn QDs. For 325 °C annealing sample, a broad wave packet with the peak less than 0.6 eV is obtained as shown in Fig. 4d. Limited by the detector of the equipment, lower energy of the spectrum cannot be acquired. The large FWHM reflects the inhomogeneous of the crystalline GeSn, and the estimated peak is also close to the bandgap extracted from the absorption spectra and calculation. Except for the broad peak, the rest of the spectrum is similar to that of the substrate. According to the above characterizations, the properties of the samples are summarized in Table 1.

In the view of CNT, whether a stable crystal nucleus can be formed depends on the difference of Gibbs free energy ΔG between the crystal nucleus G_1 and initial state G_0 of the atoms that compose of the crystal nucleus [28]. If $\Delta G < 0$, a stable crystal nucleus can be formed, while if $\Delta G > 0$, the forming crystal nucleus would transiently decompose into separated atoms as in the initial state. Take elemental semiconductor as an example. Assuming that a crystal nucleus is composed of N atoms, the ΔG can be expressed as

$$\Delta G = N\Delta\mu + \varphi \tag{1}$$

where $\Delta\mu$ presents the difference of chemical potential between the atom in the crystal nucleus and the initial state, φ presents the surface energy of the crystal nucleus. Apparently, $\Delta\mu < 0$, because a more stable state of the atoms is in the regular lattice than in the initial state with disorder. However, φ is always larger than 0 as the stable bonds are broken at the surface. Owing to a high ratio of the surface area to the volume, the ΔG is predominated by the φ in the incubation period of the crystal nucleus [21,29–33]. That is, an energy barrier is needed to be overcome if a stable nucleus is expected.

For GeSn alloys, it is more complicated as the φ would inevitably be affected by the Sn fraction. In this regard, first-principles calculation is adopted. The calculation tool used here is Vienna Ab initio Simulation Package (VASP) [34–36]. Slab models are constructed to calculate σ, the φ per unit area. Two cleavage schemes are applied to build the GeSn slabs. One leaves the Sn atoms on the surface of the slab while the other exposes the surfaces only containing Ge atoms, as shown in Fig. 5a. The grey and purple atoms represent the Ge and Sn atoms, respectively. The thickness of the vacuum layer is 10 Å. The σ with only Ge atoms is defined as σ_{Ge} and that containing Sn and Ge atoms is defined as $\sigma_{Ge\text{-}Sn}$. σ_{Ge} can be easily obtained from the GeSn slab as shown on the left of Fig. 5a, because the total surface energy of the slab is 2 times of σ_{Ge}. Hence, $\sigma_{Ge\text{-}Sn}$ can be obtained by subtracting σ_{Ge} from the total surface energy of the slab on the right of Fig. 5a. The Sn fraction of slabs in Fig. 5a is 4.16%, slabs with Sn fraction of 6.25 and 12.5% are calculated as well (their slab models are not shown here). The complete slab models with the calculated Sn fractions and the calculation details are described in Supplementary material. As shown in Fig. 5b, σ_{Ge} (blue solid rectangle and blue solid line) and $\sigma_{Ge\text{-}Sn}$ (pink solid circle and pink solid line) decrease with the increase of Sn fraction, indicating the incorporation of more Sn atoms in the lattice will result in lower surface energy. Furthermore, for a given Sn fraction, $\sigma_{Ge\text{-}Sn}$ is lower than σ_{Ge} about 0.02 eV. Accordingly, the crystal nucleus with more Sn atoms on the surface is energetically favorable in the incubation period, as the energy barrier can be well reduced. For the as deposited a-GeSn, the crystallization barrier is higher than the thermal energy supplied from the annealing temperature in the experiments. However, as the annealing time increase, Sn atoms from the Sn stripes diffused into the GeSn and gather together, facilitating the occurrence of GeSn crystal nucleus. Fig. 5c schematically shows the ΔG variation of crystal nucleus with the radius for different Sn fraction. With more Sn fraction, the energy barrier is lower as well as the critical radius $R_{nucleus}$ is smaller. As the size of the crystal nucleus reach to $R_{nucleus}$, a stable GeSn crystal nucleus is formed. After that, the surface of the crystal nucleus will reduce the energy barrier of crystallization for the surrounded a-GeSn and further induce the a-GeSn get crystalline, leading to the continuing growth of the GeSn nanocrystal. As discussed above, more Sn atoms is favored, therefore, the Sn fraction of the crystalline GeSn increase with the growth. The outer region of the nanocrystal will suffer an increasing compress strain from the inner region during the growth, as a larger lattice mismatch is produced between the outer and the inner regions. To investigate the influence induced by the compress strain, both the σ of GeSn slabs and free energy of GeSn bulks with compress strain are calculated. Here, the GeSn bulk denote the crystal part in the slab cell without the consideration of the surfaces. A limiting case is introduced that all the lattice parameters in the strained planes of the GeSn slabs and bulks are compressed to that of relaxed Ge. The tetragonal distortion methodology is applied to adjust the lattice parameters normal to the strained planes. The calculation details are described in Supplementary material. As shown in Fig. 5b, small variation is observed for σ_{Ge} and $\sigma_{Ge\text{-}Sn}$ between the relaxed and strained slabs. Nonetheless, for a given Sn fraction, the free energy of the strained GeSn bulk is higher than that of the relaxed, as shown in Fig. 5d. With the Sn fraction increase, the increment of energy enlarges significantly. As a result, the energy barrier for the growth of the GeSn nanocrystal increases and will reach the thermal energy. Once that, the GeSn nanocrystal stops growing, or in other words, be ripe.

Fig. 5e schematically illustrate the synthesis process of the GeSn QDs. During the annealing, Sn atoms from the Sn stripes diffuse into the GeSn stripes and tends to assemble randomly at places uniformly distributed in the GeSn layer, as the left of Fig. 5e shows. As the amount of Sn atoms is adequate to reduce the energy barrier for crystallization, the GeSn crystal nucleuses occurs. After that, the crystal nucleuses grow with more Sn atoms incorporated, as the middle of Fig. 5e shows. As the energy barrier heightened to reach the supplied thermal energy, the growth stops and the GeSn QDs formed. For different annealing temperature, the forming GeSn QDs are different. The decrement of energy barrier for crystallization depends on the thermal energy supplied from the annealing. Smaller decrement of energy barrier for crystallization is needed for higher annealing temperature while larger decrement is necessary for lower annealing temperature. And smaller decrement of energy barrier indicates lower Sn concentration for the formation of GeSn nucleus and vice versa. Higher Sn concentration increases the occurrence probability of crystal nucleus and leads to a higher density of the nucleus. Therefore, the area density of GeSn QDs for 275 °C annealing sample is higher than that for the 300 °C annealing sample. The relatively higher initial Sn fraction of the GeSn nucleus for lower annealing temperature will result in a higher overall Sn fraction of GeSn QDs than that for higher annealing temperature. Nonetheless, higher Sn fraction implying more compress strain, GeSn QDs for lower annealing

Table 1
Properties of GeSn stripes annealed at 275, 300 and 325 °C, respectively.

Temperature (°C)	Crystallinity of GeSn stripe (%)	Mean size/ FWHM (nm)	Sn fraction by TEM/ Absorption (%)	Area density (cm^{-2})	PL peak (eV)
275	23.1	3/2.1	44.2/44.8	2.1×10^{12}	0.787
300	32.6	5/1.7	13.6/12.8	5.5×10^{11}	0.800
325	38.3	12/5.4	8.8/7.9	–	–

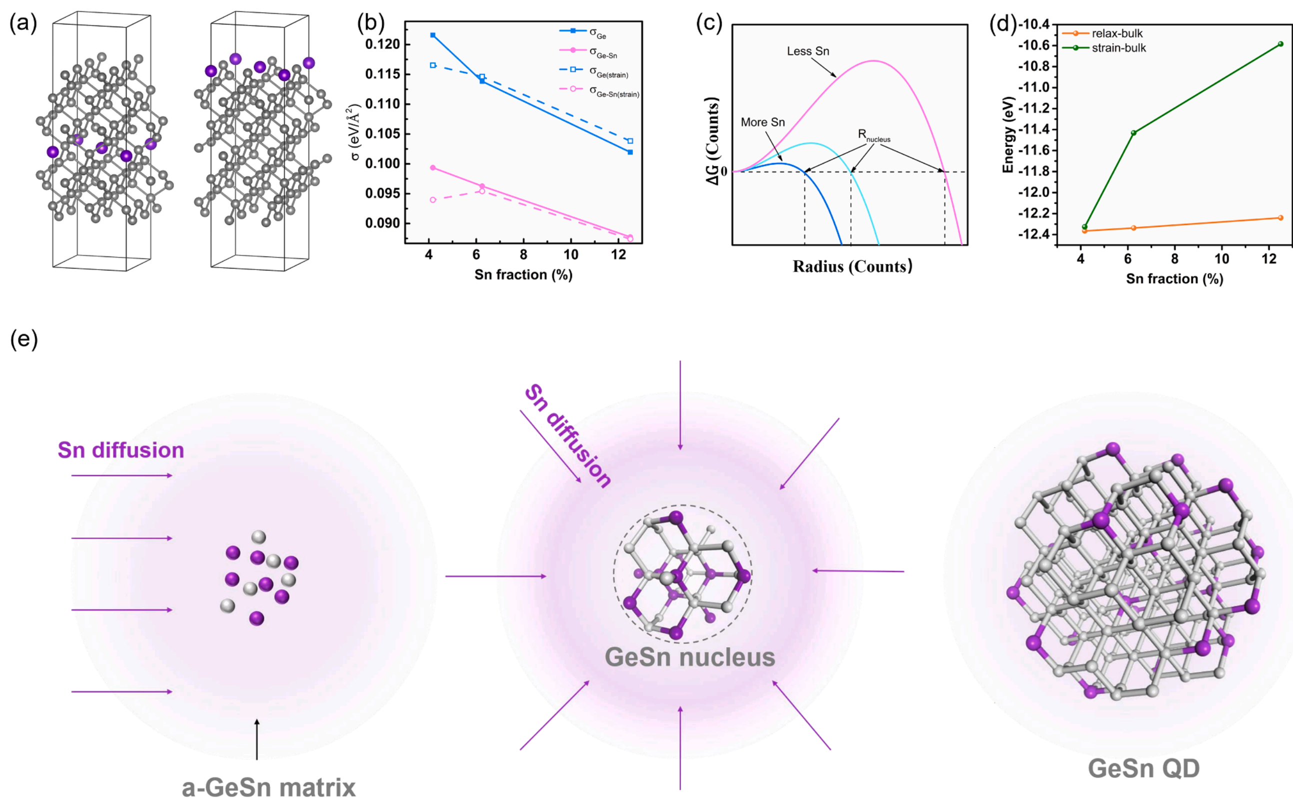

Fig. 5. (a) The structure of GeSn alloys where purple and grey atoms represent Sn and Ge elements, respectively. (b) Sn fraction dependence of surface energy per unit area. (c) The change in Gibbs free energy ΔG, versus nucleation radius R for different Sn fraction. (d) The energy of GeSn Super-cell dependence on Sn fraction. (e) Schematic illustration of the GeSn nanocrystals formation.

temperature stop growing at a smaller radius than that for higher annealing temperature. As a consequence, the average size of the GeSn QDs for 275 °C annealing sample is smaller than that for 300 °C annealing sample. As the annealing temperature increases to 325 °C, less Sn concentration is demanded and larger size of the GeSn nanocrystals is obtained, forming the local polycrystalline morphology. It should be note that a higher temperature would inevitably cause a faster diffusion then a faster formation of GeSn nanocrystals. Thus, a shorter annealing time may be adequate for the sample annealed at 325 °C.

4. Conclusion

A highly controllable method to prepare GeSn QDs in a CMOS compatible way is demonstrated in this work. The prepared GeSn QDs have ultra-high area density, narrow size distribution, and high Sn fraction, and are free of Sn segregation or precipitation. Room-temperature photoluminescence is detected for the GeSn QDs, revealing the highly efficient of light emission as well as low light loss and low non-radiative recombination rate. The area density, size, Sn fraction, and the light emission peak of the GeSn QDs can well be controlled by merely adjusting the preparation temperature. The synthesis mechanism of the GeSn QDs is comprehensively revealed with evidences provided by CNT and first-principles results. The properties of the GeSn QDs prepared in this method may be improved by optimizing several parameters such as the initial Sn content and thickness of the a-GeSn stripes, and the covering layer on the GeSn stripes. Their opto-electrical properties may also be enhanced by tuning the oxidative states with doping [37]. The feasible and CMOS compatible method to synthesis GeSn QDs with distinguished property and high controllability may provide a promising way to obtain highly efficient Si-based light emitting materials, and may further be applied in other group-IV alloys, such as SiSn, SiGeSn, SiPb, and GePb.

CRediT authorship contribution statement

Lu Zhang: Conceptualization, Methodology, Writing – original draft, Validation. **Haiyang Hong:** Investigation, Methodology, Writing – review & editing. **Kun Qian:** Visualization, Investigation. **Songsong Wu:** Software, Investigation. **Guangyang Lin:** Investigation. **Jianyuan Wang:** Investigation. **Wei Huang:** Investigation. **Songyan Chen:** Investigation. **Cheng Li:** Software, Supervision, Writing – review & editing.

Declaration of Competing Interest

The authors declare that they have no known competing financial interests or personal relationships that could have appeared to influence the work reported in this paper.

Acknowledgements

This work is supported by the National Key Research Program of China (2018YFB2200103) and National Natural Science Foundation of China (62074134).

Appendix A. Supplementary material

Supplementary data to this article can be found online at https://doi.org/10.1016/j.apsusc.2021.152249.

References

[1] A. Elbaz, D. Buca, N. von den Driesch, K. Pantzas, G. Patriarche, N. Zerounian, E. Herth, X. Checoury, S. Sauvage, I. Sagnes, A. Foti, R. Ossikovski, J.M. Hartmann, F. Boeuf, Z. Ikonic, P. Boucaud, D. Grützmacher, M. El Kurdi, Ultra-low-threshold continuous-wave and pulsed lasing in tensile-strained GeSn alloys, Nat. Photonics 14 (6) (2020) 375–382, https://doi.org/10.1038/s41566-020-0601-5.

[2] A. Elbaz, R. Arefin, E. Sakat, B. Wang, E. Herth, G. Patriarche, A. Foti, R. Ossikovski, S. Sauvage, X. Checoury, K. Pantzas, I. Sagnes, J. Chrétien, L. Casiez, M. Bertrand, V. Calvo, N. Pauc, A. Chelnokov, P. Boucaud, F. Boeuf, V. Reboud, J.-M. Hartmann, M. El Kurdi, Reduced lasing thresholds in GeSn microdisk cavities with defect management of the optically active region, ACS Photonics 7 (10) (2020) 2713–2722, https://doi.org/10.1021/acsphotonics.0c0070810.1021/acsphotonics.0c00708.s001.

[3] Y. Zhou, Y. Miao, S. Ojo, H. Tran, G. Abernathy, J.M. Grant, S. Amoah, G. Salamo, W. Du, J. Liu, J. Margetis, J. Tolle, Y. Zhang, G. Sun, R.A. Soref, B. Li, S.Q. Yu, Electrically injected GeSn lasers on Si operating up to 100 K, Optica 7 (8) (2020) 924, https://doi.org/10.1364/optica.395687.

[4] J. Chrétien, N. Pauc, F. Armand Pilon, M. Bertrand, Q.-M. Thai, L. Casiez, N. Bernier, H. Dansas, P. Gergaud, E. Delamadeleine, R. Khazaka, H. Sigg, J. Faist, A. Chelnokov, V. Reboud, J.-M. Hartmann, V. Calvo, GeSn Lasers Covering a Wide Wavelength Range Thanks to Uniaxial Tensile Strain, ACS Photonics 6 (10) (2019) 2462–2469.

[5] Y. Zhou, W. Dou, W. Du, S. Ojo, H. Tran, S.A. Ghetmiri, J. Liu, G. Sun, R. Soref, J. Margetis, J. Tolle, B. Li, Z. Chen, M. Mortazavi, S.-Q. Yu, Optically pumped GeSn lasers operating at 270 k with broad waveguide structures on Si, ACS Photonics 6 (6) (2019) 1434–1441, https://doi.org/10.1021/acsphotonics.9b0003010.1021/acsphotonics.9b00030.s001.

[6] D. Stange, N. von den Driesch, T. Zabel, F. Armand-Pilon, D. Rainko, B. Marzban, P. Zaumseil, J.-M. Hartmann, Z. Ikonic, G. Capellini, S. Mantl, H. Sigg, J. Witzens, D. Grützmacher, D. Buca, GeSn/SiGeSn heterostructure and multi quantum well lasers, ACS Photonics 5 (11) (2018) 4628–4636, https://doi.org/10.1021/acsphotonics.8b0111610.1021/acsphotonics.8b01116.s001.

[7] H. Hong, L. Zhang, K. Qian, Y. An, C. Li, J. Li, S. Chen, W. Huang, J. Wang, S. Zhang, Limitation of bulk GeSn alloy in the application of a high-performance laser due to the high threshold, Opt. Express 29 (1) (2021) 441, https://doi.org/10.1364/OE.409899.

[8] I.A. Fischer, C.J. Clausen, D. Schwarz, P. Zaumseil, G. Capellini, M. Virgilio, M. C. da Silva Figueira, S. Birner, S. Koelling, P.M. Koenraad, M.R.S. Huang, C. T. Koch, T. Wendav, K. Busch, J. Schulze, Composition analysis and transition energies of ultrathin Sn-rich GeSn quantum wells, Phys. Rev. Mater. 4 (2) (2020), https://doi.org/10.1103/PhysRevMaterials.4.024601.

[9] L. Peng, X. Li, Z. Liu, X. Liu, J. Zheng, C. Xue, Y. Zuo, B. Cheng, Horizontal GeSn/Ge multi-quantum-well ridge waveguide LEDs on silicon substrates, Photonics Res. 8 (6) (2020) 899, https://doi.org/10.1364/prj.386996.

[10] L. Peng, X. Li, J. Zheng, X. Liu, M. Li, Z. Liu, C. Xue, Y. Zuo, B. Cheng, Room-temperature direct-bandgap electroluminescence from type-I GeSn/SiGeSn multiple quantum wells for 2 μm LED, J. Lumin. 228 (March) (2020), 117539, https://doi.org/10.1016/j.jlumin.2020.117539.

[11] A.C. Meng, M.R. Braun, Y. Wang, S. Peng, W. Tan, J.Z. Lentz, M. Xue, A. Pakzad, A. F. Marshall, J.S. Harris, W. Cai, P.C. McIntyre, Growth mode control for direct-gap core/shell Ge/GeSn nanowire light emission, Mater. Today 40 (November) (2020) 101–113, https://doi.org/10.1016/j.mattod.2020.05.019.

[12] S. Assali, R. Bergamaschini, E. Scalise, M.A. Verheijen, M. Albani, A. Dijkstra, A. Li, S. Koelling, E.P.A.M. Bakkers, F. Montalenti, L. Miglio, Kinetic control of morphology and composition in Ge/GeSn core/shell nanowires, ACS Nano 14 (2) (2020) 2445–2455, https://doi.org/10.1021/acsnano.9b0992910.1021/acsnano.9b09929.s001.

[13] H. Hijazi, M. Zeghouane, F. Bassani, P. Gentile, B. Salem, V.G. Dubrovskii, Impact of droplet composition on the nucleation rate and morphology of vapor-liquid-solid GeSn nanowires, Nanotechnology 31 (40) (2020) 405602, https://doi.org/10.1088/1361-6528/ab99f6.

[14] S. Assali, A. Dijkstra, A. Li, S. Koelling, M.A. Verheijen, L. Gagliano, N. von den Driesch, D. Buca, P.M. Koenraad, J.E.M. Haverkort, E.P.A.M. Bakkers, Growth and Optical Properties of Direct Band Gap Ge/Ge 0.87 Sn 0.13 Core/Shell Nanowire Arrays, Nano Lett. 17 (3) (2017) 1538–1544.

[15] A. Slav, C. Palade, C. Logofatu, I. Dascalescu, A.M. Lepadatu, I. Stavarache, F. Comanescu, S. Iftimie, S. Antohe, S. Lazanu, V.S. Teodorescu, D. Buca, M. L. Ciurea, M. Braic, T. Stoica, GeSn nanocrystals in $GeSnSiO_2$ by magnetron sputtering for short-wave infrared detection, ACS Appl. Nano Mater. 2 (6) (2019) 3626–3635, https://doi.org/10.1021/acsanm.9b0057110.1021/acsanm.9b00571.s001.

[16] V. Tallapally, T.A. Nakagawara, D.O. Demchenko, Ü. Özgür, I.U. Arachchige, Ge_{1-X}Snx alloy quantum dots with composition-tunable energy gaps and near-infrared photoluminescence, Nanoscale 10 (43) (2018) 20296–20305, https://doi.org/10.1039/c8nr04399j.

[17] S.A. Hafiz, R.J.A. Esteves, D.O. Demchenko, I.U. Arachchige, Ü. Özgür, Energy gap tuning and carrier dynamics in colloidal $Ge_{1-X}Sn_x$ quantum dots, J. Phys. Chem. Lett. 7 (17) (2016) 3295–3301, https://doi.org/10.1021/acs.jpclett.6b0133310.1021/acs.jpclett.6b01333.s001.

[18] Q.i. Yang, X. Zhao, X. Wu, M. Li, Q. Di, X. Fan, J. Zhu, X. Song, Q. Li, Z. Quan, Facile synthesis of uniform Sn_{1-x} Ge_x alloy nanocrystals with tunable bandgap, Chem. Mater. 31 (7) (2019) 2248–2252, https://doi.org/10.1021/acs.chemmater.8b0415310.1021/acs.chemmater.8b04153.s001.

[19] K. Ramasamy, P.G. Kotula, N. Modine, M.T. Brumbach, J.M. Pietryga, S.A. Ivanov, Cubic SnGe nanoalloys: beyond thermodynamic composition limit, Chem. Commun. 55 (19) (2019) 2773–2776, https://doi.org/10.1039/c8cc07570k.

[20] H. Okamoto, K. Takita, K. Tsushima, T. Tawara, K. Tateno, G. Zhang, H. Gotoh, Low-temperature formation of GeSn nanodots by Sn mediation, Jpn. J. Appl. Phys. 58 (SD) (2019) SDDG09, https://doi.org/10.7567/1347-4065/ab14d0.

[21] A.A. Tonkikh, N.D. Zakharov, A.A. Suvorova, C. Eisenschmidt, J. Schilling, P. Werner, Cubic phase Sn-rich GeSn nanocrystals in a Ge matrix, Cryst. Growth Des. 14 (4) (2014) 1617–1622, https://doi.org/10.1021/cg401652f.

[22] L. Zhang, H. Hong, C. Li, S. Chen, W. Huang, J. Wang, H. Wang, High-Sn fraction GeSn quantum dots for Si-based light source at 1.55 μm, Appl. Phys. Express 12 (5) (2019) 055504, https://doi.org/10.7567/1882-0786/ab0993.

[23] L. Zhang, H. Hong, C. Yu, C. Li, S. Chen, W. Huang, J. Wang, H. Wang, Poly-GeSn junctionless thin-film transistors on insulators fabricated at low temperatures via pulsed laser annealing, Phys. Status Solidi - Rapid Res. Lett. 13 (11) (2019) 1–6, https://doi.org/10.1002/pssr.201900420.

[24] L. Zhang, H.-Y. Hong, Y.-S. Wang, C. Li, G.-Y. Lin, S.-Y. Chen, W. Huang, J.-Y. Wang, Formation of high-Sn content polycrystalline GeSn films by pulsed laser annealing on co-sputtered amorphous GeSn on Ge substrate, Chinese Phys. B 26 (11) (2017) 116802, https://doi.org/10.1088/1674-1056/26/11/116802.

[25] V. Neimash, V. Poroshin, P. Shepeliavyi, V. Yukhymchuk, V. Melnyk, A. Kuzmich, V. Makara, A.O. Goushcha, Tin induced a-Si crystallization in thin films of Si-Sn alloys, J. Appl. Phys. 114 (21) (2013) 213104, https://doi.org/10.1063/1.4837661.

[26] H. Li, J. Brouillet, A. Salas, I. Chaffin, X. Wang, J. Liu, Low temperature geometrically confined growth of pseudo single crystalline GeSn on amorphous layers for advanced optoelectronics, ECS Trans. 64 (819) (2014), https://doi.org/10.1149/06406.0819ecst.

[27] J.D. Gallagher, C.L. Senaratne, J. Kouvetakis, J. Menéndez, Compositional dependence of the bowing parameter for the direct and indirect band gaps in Ge1−ySny alloys, Appl. Phys. Lett. 105 (14) (2014) 142102, https://doi.org/10.1063/1.4897272.

[28] C.N. Nanev, Theory of nucleation, second ed., vol. 1, B.V. Elsevier, 2015. https://doi.org/10.1016/B978-0-444-56369-9.00007-1.

[29] P.R. Ohodnicki Jr., D.E. Laughlin, M.E. McHenry, M. Widom, Application of classical nucleation theory to phase selection and composition of nucleated nanocrystals during crystallization of Co-rich (Co, Fe)-based amorphous precursors, Acta Mater. 58 (14) (2010) 4804–4813, https://doi.org/10.1016/j.actamat.2010.05.015.

[30] E. Clouet, E. Clouet, N. Processes, S.L.S.A.S.M. Hand-, E. Clouet, Modeling of Nucleation Processes To cite this version : HAL Id : hal-00449858 Modeling of Nucleation Processes, 22 (2010) 203–219.

[31] E. Clouet, M. Nastar, A. Barbu, C. Sigli, G. Martin, Precipitation in Al-Zr-Sc alloys: A comparison between kinetic Monte Carlo, cluster dynamics and classical nucleation theory, in: Proc. an Int. Conf. Solid-Solid Phase Transform. Inorg. Mater., vol. 2, 2005, pp. 683–703.

[32] P.E. L'vov, V.V. Svetukhin, Stochastic simulation of nucleation in binary alloys, Model. Simul. Mater. Sci. Eng. 26 (4) (2018) 045001, https://doi.org/10.1088/1361-651X/aaaed8.

[33] E. Clouet, M. Nastar, Classical nucleation theory in ordering alloys precipitating with L 12 structure, Phys. Rev. B - Condens. Matter Mater. Phys. 75 (2007) 1–4, https://doi.org/10.1103/PhysRevB.75.132102.

[34] G. Kresse, J. Hafner, Ab initio molecular dynamics for liquid metals, Phys. Rev. B 47 (1) (1993) 558–561.

[35] G. Kresse, J. Furthmüller, Efficiency of ab-initio total energy calculations for metals and semiconductors using a plane-wave basis set, Comput. Mater. Sci. 6 (1) (1996) 15–50.

[36] G. Kresse, J. Furthmüller, Efficient iterative schemes for ab initio total-energy calculations using a plane-wave basis set, Phys. Rev. B 54 (16) (1996) 11169–11186.

[37] Z. Shu, Y. Cai, Substitutional doped GeSe: tunable oxidative states with strain engineering, J. Mater. Chem. C 8 (39) (2020) 13655–13667, https://doi.org/10.1039/D0TC03272G.